



Ultrasonic guided wave imaging with deep learning: Applications in corrosion mapping

Xiaocen Wang^a, Min Lin^{a,b}, Jian Li^a, Junkai Tong^a, Xinjing Huang^a, Lin Liang^c, Zheng Fan^d, Yang Liu^{a,*}

^a State Key Laboratory of Precision Measuring Technology and Instruments, Tianjin University, 92 Weijin Road, Tianjin 300072, China

^b Department of Mechanical Engineering, University of Wyoming, Laramie, WY 82071, USA

^c Schlumberger-Doll Research, One Hampshire St, Cambridge, MA 02139, USA

^d School of Mechanical and Aerospace Engineering, Nanyang Technological University, 50 Nanyang Avenue, Singapore 639798, Singapore



ARTICLE INFO

Keywords:

Ultrasonic guided wave imaging
Convolutional neural network
Quantitative evaluation of corrosion damage
Dispersion curve

ABSTRACT

In this paper, a rapid guided wave imaging method based on convolutional neural network (CNN) is proposed to quantitatively evaluate the corrosion damage. The method contains offline training and online imaging. The purpose of offline training is to establish the relationship between the detection signals and the velocity map based on forward modeling data. In the step of online imaging, the velocity map can be predicted in real-time with the detection signals fed into the trained model. Then, the remaining thickness of corroded structures can be estimated according to the dispersion curves of a specific guided wave mode. Numerical results indicate that the average correlation coefficients of the optimal model are respectively 0.9493, 0.9273, and 0.9262 in training, validation, and testing. The success rate of applying the optimal model to the testing set is 82.73% if the correlation coefficient greater than or equal to 0.9 is used as the criterion of successful corrosion imaging, which proves the excellent imaging performance. Furthermore, the imaging speed is verified and the damage reconstruction of 4000 samples is done within 3 s. The imaging method also can be used to detect the position of small corrosion damage. For a noise-contaminated dataset, the size and location can be accurately predicted, albeit damage sizing is rather challenging. Moreover, experiments have been carried out and the correlation coefficient between the true velocity map and the imaging results is 0.9109, which proves the imaging method can be applied in practice.

1. Introduction

Corrosion is an irreversible material damage phenomenon caused by the interaction of materials with surrounding media, that leads to the inherent properties degradation of materials [1]. Corrosion involves many industries, such as petrochemicals, aerospace, transportation, etc. [2–4]. Reduced service life is a common phenomenon, and catastrophic accidents may occur due to component failure caused by corrosion [5]. Especially in the fields of chemicals, oil and natural gas, corrosion can also cause environmental issues and energy waste. Due to the significant impact on safety, environment, and economy, corrosion detection is imperative and has important guiding significance for the implementation of reasonable prevention strategies.

* Corresponding author.

E-mail address: ultrasonicslab@tju.edu.cn (Y. Liu).

A variety of Nondestructive Testing (NDT) technologies have been explored for corrosion detection in recent years. Fluorescent compounds corrosion detection technology is based on the change of fluorescence properties when fluorescent compounds recombining with a specific metal ion under different oxidation and reduction states. This method has high sensitivity and is suitable for corrosion detection of external structures and coatings [6–8]. Optical fiber sensing is a convenient corrosion monitoring method [9,10]. The dielectric cladding of optical waveguide is partially replaced by corrosion sensitive film and the corrosion can be monitored according to the output optical power. Optical fiber sensors can be used in harsh environments, but they must cover the object. Acoustic emission corrosion detection technology is not limited by materials, because all materials have acoustic emission characteristics [11–13]. It receives and processes the acoustic emission characteristics of materials through sensors and signal processing so that the position and size of corrosion can be detected. All of these methods can only locate and roughly estimate corrosion severity, while corrosion imaging is still challenging. Ultrasound is a crucial NDT mean and the ultrasonic imager has been commercialized, which can detect the subsurface corrosion, delamination, voids, cracks of material with high resolution [14–17].

Compared with traditional ultrasonic Nondestructive Evaluation (NDE) methods, ultrasonic guided wave (UGW) is particularly advantageous for large area detection and tomography. Sriramadasu *et al.* presented a methodology based on differential time of arrival of various scattered wave modes to detect corrosion in rebar [18]. According to the damage index, the axial extent and intensity of pitting corrosion in rebars can be monitored. For an arbitrary position corrosion, a differential time of arrival methodology is proposed to identify the location of the pitting corrosion. Sharma *et al.* used UGW to monitor invisible corrosion in concrete. By comparing the changes in the amplitude and characteristics of transmitted signals, the damage caused by corrosion can be quantified [19]. Farhidzadeh *et al.* proposed reference-free corrosion diagnosis in steel strands using guided waves [20]. The method can quantitatively evaluate corrosion damage of pre-stressing steel strands by combining dispersion curves, continuous wavelet transform, and wave velocity measurements. Mažeika *et al.* applied guided ultrasonic waves for inspection of the fuel tank's floor, the ultrasonic transmitters and receivers are simply placed on the bottom edge of the tank without emptying the tank [21]. Experimental results show that the non-uniformities spatial distribution of tank floor can be reconstructed in a real 8 m diameter tank. Rao *et al.* presented a UGW reconstruction algorithm based on full waveform inversion (FWI), the corrosion thicknesses can be reconstructed and the corrosion positions closely resemble the actual sites [22]. In order to address image quality degradation caused by missing viewing angles, they adopted a regularization method to synthesize the missing components. Experimental results indicated that the artifacts can be reduced and reconstruction accuracy is improved [23]. Huthwaite *et al.* extended the hybrid algorithm for robust breast ultrasound tomography (HARBUT) to guided wave tomography [24]. This method can improve the accuracy reconstruction of defects from corrosion by iterating HARBUT. However, the imaging resolution can be further improved taking higher order scatterings into account. Willey *et al.* reported the application of guided wave tomography (GWT) to pipe monitoring based on Electromagnetic Acoustic Transducers (EMATs). This method improved the image resolution and depth estimation accuracy, and solved the typical thermal fluctuations encountered during continuous monitoring [25]. Park *et al.* applied the probabilistic inspection of damage (RAPID) algorithm to defect imaging in curved surfaces like aircraft [26]. The signals are compared according to the damage index (DI) of the signal difference coefficient (SDC), and then the damage index of each spatially distributed transducers is added to realize damage imaging. He *et al.* improved the traditional reverse-time migration (RTM) method and proposed a least-squares RTM method [27]. This method improves shape reconstructions and reduces artifacts, which is promising for damage imaging in plate-like structures. The above-mentioned methods can be used to evaluate the degree of corrosion damage, and some tomography algorithms, such as FWI, HARBUT, RAPID, RTM and their variants can be used to image corrosion. However, these existing UGW tomography algorithms that are not based on deep learning still have some problems, for example, imaging speed and quality need to be further improved. In recent years, many studies have applied deep learning to UGW detection. Xu *et al.* proposed guided wave-convolutional neural network to diagnose fatigue crack and 19 crack levels can be evaluated [28]. Liu *et al.* presented a notch crack damage evaluation method based on CNN for thin plate structure using guided wave. This method can detect the occurrence of damage and its location [29]. The two methods can only locate the damages and evaluate the damage level, but cannot image damage visually. Song *et al.* combines ultrasonic beamforming and deep learning to realize super-resolution visualization of subwavelength defects [30]. The raw defect image can be created by the classic TFM and the image resolution can be improved by deep learning. Afterwards, in order to solve the problem about the diffraction limit and dispersion of guided waves, noncontact super-resolution guided wave array imaging of subwavelength defects using a multiscale deep learning approach is proposed [31]. The global detection network is used to detect subwavelength defects in the original low-resolution guided wave beamforming imaging. Then, the subwavelength-scale fine structural details of the detected defects can be highlighted by the local super-resolution network. These technologies mainly focus on super-resolution imaging based on traditional UGW imaging. In general, ultrasonic guided wave imaging technology with small reconstruction error and high reconstruction speed is still a challenge.

In this paper, an ultrasonic guided wave inversion framework based on a one-dimensional convolutional neural network is established for quantitative corrosion imaging with small reconstruction error and high reconstruction speed. The relationship between the detection signals and the velocity map is established so as to deduce the corrosion depth by the dispersion curves. The paper is organized as follows. Section II elaborates the principle of forward modeling of 2D wave equation, the convolutional neural network, and velocity to thickness transformation. Section III presents numerical experiments, laboratory experiment and experiment results. The number of alternating convolutional and pooling layers and fully connected (FC) layer nodes are adjusted to obtain the optimal imaging model. Besides, the influence of corrosion size on imaging reconstruction error is studied and the anti-noise ability of the model is tested. Laboratory experiments have been conducted to demonstrate the practicability of the method. Section IV draws conclusions.

2. Principle

This section introduces the principle of UGW imaging based on deep learning for quantitative corrosion damage evaluation. The workflow contains forward modeling, velocity map inversion of corrosion damage and velocity to thickness transformation.

2.1. Forward modeling of 2D wave equation

Forward modeling is the derivation of the distribution properties of the field from the properties of the source, which means the wavefield can be obtained according to the wave equations when the physical properties of the plate-like structure are known. Therefore, forward modeling is used to generate wavefield data according to known corrosion damage in plate-like structure so as to build the numerical corrosion damage database, which is the data preparation stage of UGW imaging.

In the 2D space-time domain, the elastic wave equations for isotropic materials are written as [32]:

$$K(x)\mathbf{u}(x, t) + \gamma(x)\dot{\mathbf{u}}(x, t) + M(x)\ddot{\mathbf{u}}(x, t) = P(x, t) \quad (1)$$

where $M(x)$ and $K(x)$ refer to the mass matrix and the stiffness matrix, respectively. $\mathbf{u}(x, t)$ is the displacement wavefield and $P(x, t)$ represents the point source. The spatial coordinate is denoted by x , and the time by t . The second term, $\gamma(x)\dot{\mathbf{u}}(x, t)$, on the left-hand side is the damping term that works as the absorbing layers in the boundaries. $\gamma(x)$ represents the damping parameter. The damping term prevents the wave reflection from the boundaries by absorbing the energy of waves propagating in the damping layers.

Forward modeling formula in the frequency domain can be obtained by taking the temporal Fourier transform of Eq. (1), which results in [32]:

$$K\mathbf{u}(x, \omega) + i\omega\gamma\mathbf{u}(x, \omega) - \omega^2 M\mathbf{u}(x, \omega) = P(x, \omega) \quad (2)$$

where ω is the angular frequency. After some arrangement, Eq. (2) can be further simplified into a compact form:

$$E(x, \omega)\mathbf{u}(x, \omega) = P(x, \omega) \quad (3)$$

Here, we use the substitution of $E = -\omega^2 M + i\omega\gamma + K$ and E is the complex impedance matrix. $\mathbf{u}(x, \omega)$ and $P(x, \omega)$ are the Fourier transform of $\mathbf{u}(x, t)$ and $P(x, t)$, respectively.

Several numerical techniques can be applied to compute the wavefield \mathbf{u} in both time and frequency domains, including finite difference, finite element, and finite volume methods [32–34]. Among them, finite difference method is the most widely used one to solve 2D wave equations due to its computational efficiency and easy implementation.

In finite differences, the wave equation can be computed by first using lower and upper (LU) decomposition of the complex impedance matrix. The LU factors can then be used by every source in the forward modeling. The LU decomposition only needs to perform once, which effectively reduces the computation time [32].

Model parameters, such as velocity, are included in Eq. (3) implicitly. For illustration purpose, we write the displacement wavefield \mathbf{u} and velocity wavefield c as a nonlinear relationship:

$$\mathbf{u} = \mathbf{G}(c) \quad (4)$$

where \mathbf{G} denotes the forward modeling operator, and $c(x)$ is the spatially varying wave velocity.

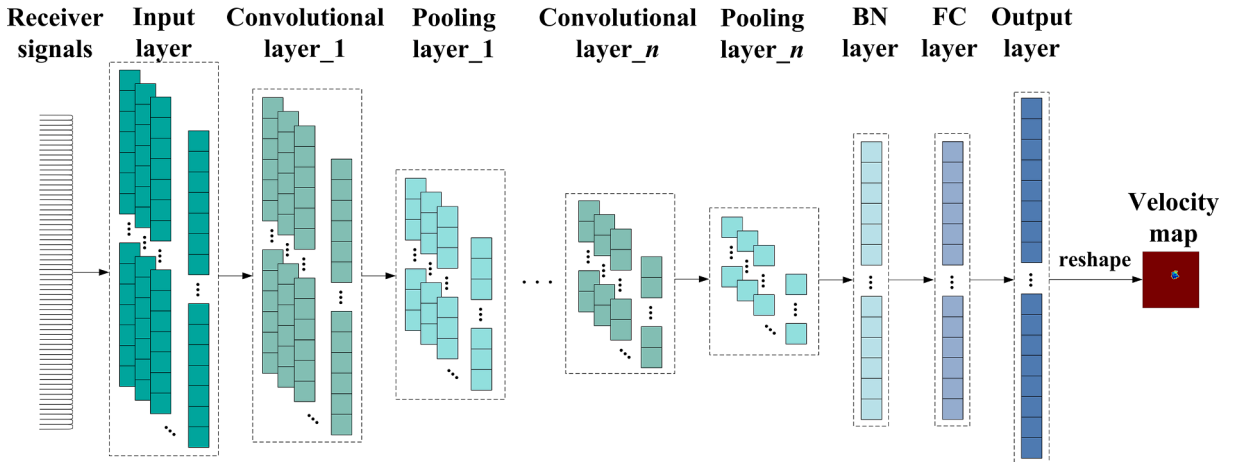


Fig. 1. A classical architecture of 1D-CNN consists input layer, convolution layers, pooling layers, BN layers, FC layers and output layer. By stacking layers with various functions, the velocity map can be reconstructed.

2.2. The principle of 1D-CNN

The purpose of this study is to achieve small reconstruction error and high reconstruction speed corrosion quantitative imaging based on UGW, which means constructing 2D corrosion images from detection signals from the receivers. 1D-CNN is utilized to discover the direct mapping relationship between the input detection signals and the output velocity map. The base network architecture is firstly built to as shown in Fig. 1, including the input layer, convolutional layers, pooling layers, batch normalization layers and FC layers. Since the network structure and parameters have a great influence on the imaging quality, the structure and parameters should be adjusted so as to determine the optimal model. The operation details of velocity map inversion based on CNN are as follows.

The original detection signals $d_{64 \times 64}$ from 64 receivers are flattened into the one-dimensional vectors $d = [d_1, d_2, \dots, d_{4096}]$, and then directly fed into the input layer. Adjacent to the input layer, the convolutional layer is connected for feature extraction of flattened original detection signals and the convolution operation follows Eq. (5) [35]:

$$d_j^l = \sum_{i=1}^{n_l-1} \text{conv1D}\left(w_{ij}^{l-1}, d_i^{l-1}\right) + b_j^l \quad (5)$$

where d_j^l is the j^{th} neuron in the l^{th} layer, w_{ij}^{l-1} is the kernel weight connecting the i^{th} neuron in the $l-1^{\text{th}}$ layer to the j^{th} neuron in the l^{th} layer, d_i^{l-1} is the i^{th} neuron in the $l-1^{\text{th}}$ layer, b_j^l is the j^{th} neuron bias in the l^{th} layer.

In order to enhance the nonlinear expression, ensure computation speed and avoid dead Rectified Linear Unit (ReLU), leaky ReLU is introduced after convolution operation [36].

Since some adjacent elements of the flat one-dimensional detection signals have similar values, the adjacent outputs of convolutional layer also have similar values which may result in the output redundancy. A max pooling layer is added after the convolutional layer to solve this problem, which can reduce the parameters in the subsequent layers [37]. The operation follows the equation:

$$m_p^{l+1} = \max[\hat{d}_1^l, \hat{d}_2^l, \dots, \hat{d}_z^l] \quad (6)$$

where m_p^{l+1} is the p^{th} output in the $(l+1)^{\text{th}}$ pooling layer, $[\hat{d}_1^l, \hat{d}_2^l, \dots, \hat{d}_z^l]$ is a vector containing all the output of l^{th} layer, $\max(\cdot)$ is the maximum.

Multiple convolutional layers and pooling layers alternately stack to form the core of CNN architecture. The features extracted by convolution and pooling operations are transferred to Batch Normalization (BN) layer for training acceleration and generalization ability improvement [37]. The mean μ_B and variance σ_B^2 of the mini-batch $[m_1^{l+1}, m_2^{l+1}, \dots, m_y^{l+1}]$ in the $(l+1)^{\text{th}}$ layer should be calculated and the mini-batch is normalized as the following equation:

$$\hat{m}_p^{l+1} = \frac{m_p^{l+1} - \mu_B}{\sqrt{\sigma_B^2 + \alpha}} \quad (7)$$

where α is used to avoid a divisor of zero.

The parameters φ and β are introduced to shift and scale so as to retain the extracted features. Therefore, the normalized mini-batch is transformed as:

$$s_q = \varphi \hat{m}_p^{l+1} + \beta \equiv \text{BN}_{\varphi, \beta}(m_p^{l+1}) \quad (8)$$

where φ is shift variable, β is scale variable.

After BN normalization, the first FC layer is connected for feature flattening. The purpose of network training is to establish the relationship between the detection signals and the velocity map, which can be considered as a regression task. Therefore, *sigmoid* is utilized as activation function in the output layer.

The process of network training is to minimize the cost function by adjusting the model parameters and the cost function can be defined as:

$$MSE(v_q, s_q) = \frac{1}{n \times n} \sum_{q=1}^{n \times n} \|v_q - s_q\|^2 \quad (9)$$

where *MSE* represents mean square error, v_q is the flat velocity map, s_q is the output of *sigmoid* function and its range is $(0, 1)$.

In order to determine the optimal parameters of CNN, adaptive moment estimation (Adam) algorithm replaces traditional gradient descent method to accelerate network training and avoid overfitting in offline training [38]. Adam algorithm is a first-order optimization algorithm which combines Momentum algorithm and RMSProp algorithm, and is used to update the kernel weight and bias of CNN efficiently. When the L2 norm is minimum, the flat velocity map predicted by the network is close to the flat true velocity map. The optimal parameters kernel weight w and bias b of the network are figured out. Finally, the flat velocity map from the output layer should be reshaped and reverted to a 2D velocity map.

2.3. Velocity to thickness transformation

In order to determine the remaining thickness of plate-like structure, the velocity map should be transformed to thickness map. UGWs of symmetric modes and antisymmetric modes exist in isotropic materials. Eqs. (10) and (11) are the Rayleigh-Lamb frequency equations for symmetric modes and antisymmetric modes, respectively and the solutions of Rayleigh-Lamb frequency equations are so called dispersion curves, which can be used to convert phase velocity map to corresponding thickness map [39].

$$\frac{\tan(Qh)}{\tan(Ph)} = -\frac{4k^2PQ}{(Q^2 - k^2)^2} \quad (10)$$

$$\frac{\tan(Qh)}{\tan(Ph)} = -\frac{(Q^2 - k^2)^2}{4k^2PQ} \quad (11)$$

where h denotes the thickness. P and Q are frequency dependent variables, which are defined as:

$$P^2 = \left(\frac{\omega}{c_L}\right)^2 - k^2 \quad \text{and} \quad Q^2 = \left(\frac{\omega}{c_T}\right)^2 - k^2 \quad (12)$$

where k is the wavenumber. c_L and c_T are the longitudinal and shear velocities, respectively. The phase velocity c_p of a certain Lamb wave mode can be represented as:

$$c_p = \lambda\omega/2\pi \quad (13)$$

where λ is the wavelength. The details to solve Eq. (11) by using numerical methods can be found in the textbook [39].

For isotropic materials, the thickness map \mathbf{h} is related to both phase velocity map c_p and frequency ω . Under a certain excitation frequency and a selected Lamb mode, thickness is only a function of phase velocity. Therefore, we can write the general relationship between thickness and velocity as:

$$\mathbf{h} = \mathbf{H}(c_p) \quad (14)$$

where \mathbf{H} is the transformation operator.

3. Numerical EXPERIMENT AND RESULTS

3.1. Numerical experiment setup

Fig. 2 shows the geometric model diagram in simulation and the simulation parameters are listed in **Table 1**. All the numerical experiments are conducted on a 1000 mm × 1000 mm aluminum plate with thickness of 10 mm. The material parameters in the simulation are set as: density $\rho = 2.7 \text{ g} \cdot \text{cm}^{-3}$, Poisson's ratio $\gamma = 0.33$, Young's modulus $E = 70.8 \text{ GPa}$. 64 transducers are arranged in a uniform circular array with a diameter of 0.7 m, which can be used as both transmitters and receivers. Ricker wavelet is used as the source excitation. The transmitting-receiving criterion is that 64 transducers transmit in sequence and the ultrasonic waves are recorded by all the transducers. Corrosion damages with different shapes are generated by the PC program at random position inside the circular transducer array. The diameter of corrosion ranges from 0 mm to 300 mm and the depth ranges from 0 mm to 3 mm.

In forward modeling, the 1000 mm × 1000 mm aluminum plate is discretized into 500 × 500 grids and the grid spacing is 2 mm. According to frequency selection criterion, the frequency for forward modeling is set as 50 kHz [40]. Finally, original detection signals

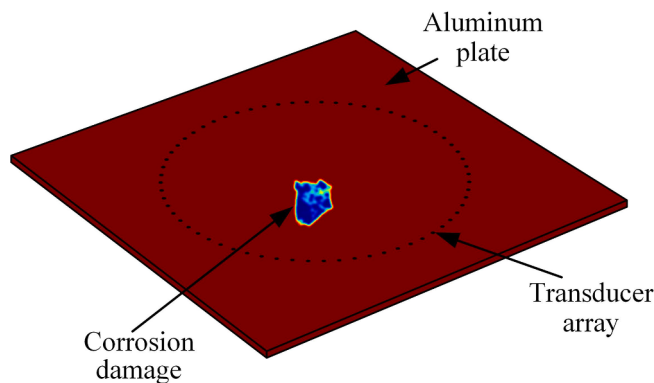


Fig. 2. The geometric model diagram in simulation. 64 transducers are arranged in uniform circular array and both the shape and position of corrosion damage are random.

Table 1

Summary of simulation parameters.

Aluminum plate	Size 1000 mm × 1000 mm × 10 mm	Density 2.7 g · cm ⁻³	Poisson's ratio 0.33	Young's modulus 70.8 GPa
Transducer layout	Diameter 0.7 m	Number 64	Shape of array a uniform circular array	
Corrosion damage	Position random (inside the circular transducer array)	Diameter 0 mm–300 mm	Depth 0 mm–3 mm	Shape irregular
Grid	Size 500 × 500	Grid spacing 2 mm		
Excitation signal	Type Ricker wavelet	Mode A0	Frequency 50 kHz	

can be acquired by space-frequency forward modeling and the size of original detection signals is 64×64 for each forward modeling.

According to the phase velocity dispersion curve in Fig. 3, the pure A0 mode can be excited in the aluminum plate when the normal displacement excitation is about 50 kHz [39]. Besides, A0 mode is sensitive to the thickness variation around 50 kHz as the phase velocity is highly dispersed in the region. Therefore, the center frequency f_c of Ricker wavelet is determined as 50 kHz.

3.2. Numerical experiment dataset preprocessing

Due to the difference between the detection system and the parameters settings, the acquired detection signals are greatly various, especially in terms of amplitude. Therefore, all the data should be preprocessed by min–max normalization to eliminate the difference between the detection system and the parameters settings. In order to match the range of sigmoid function in the output layer, the true velocity maps should also be normalized to limit the range to (0, 1). The min–max normalization is as follows:

$$\begin{aligned} x_{norm} &= \frac{(x - x_{min})}{x_{max} - x_{min}} \\ v_{norm} &= \frac{(v - v_{min})}{v_{max} - v_{min}} \end{aligned} \quad (15)$$

where x_{norm} and v_{norm} are the normalized detection signals and velocity maps, x and v are the detection signals and true velocity maps, x_{min} and x_{max} are the minimum and maximum in detection signals. Theoretically, v_{min} and v_{max} are the minimum and maximum in true velocity maps, but the values are not available. According to the corrosion depth range and thickness of aluminum plate, the remaining thickness range of aluminum plate can be determined as 7 mm – 10 mm. The corresponding phase velocity range is 1.644 km/s – 1.878 km/s, as shown in dispersion curve of aluminum plate. Therefore, v_{min} and v_{max} are respectively set as 1.644 and 1.878. Besides, the true velocity maps are down-sampled to 250×250 by selecting points of velocity maps alternately for training acceleration.

Fig. 4a–c show the typical true velocity maps, in which the color bar represents the velocity of each point and the unit is km/s. In order to enrich the dataset for better imaging performance, the corruptions with varying depths, shapes, sizes, and locations are generated on an aluminum plate. After normalization, the true velocity is limited to (0, 1), as shown in Fig. 4d–f. The data set contains 20,000 samples, and the allocation proportion of training set, validation set, and testing set is 6:2:2.

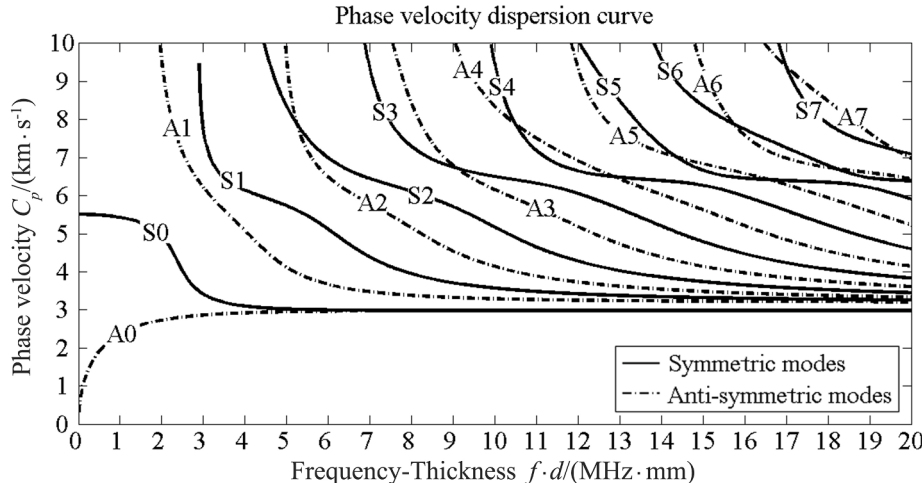


Fig. 3. The phase velocity dispersion curve of aluminum plate with 10 mm thickness.

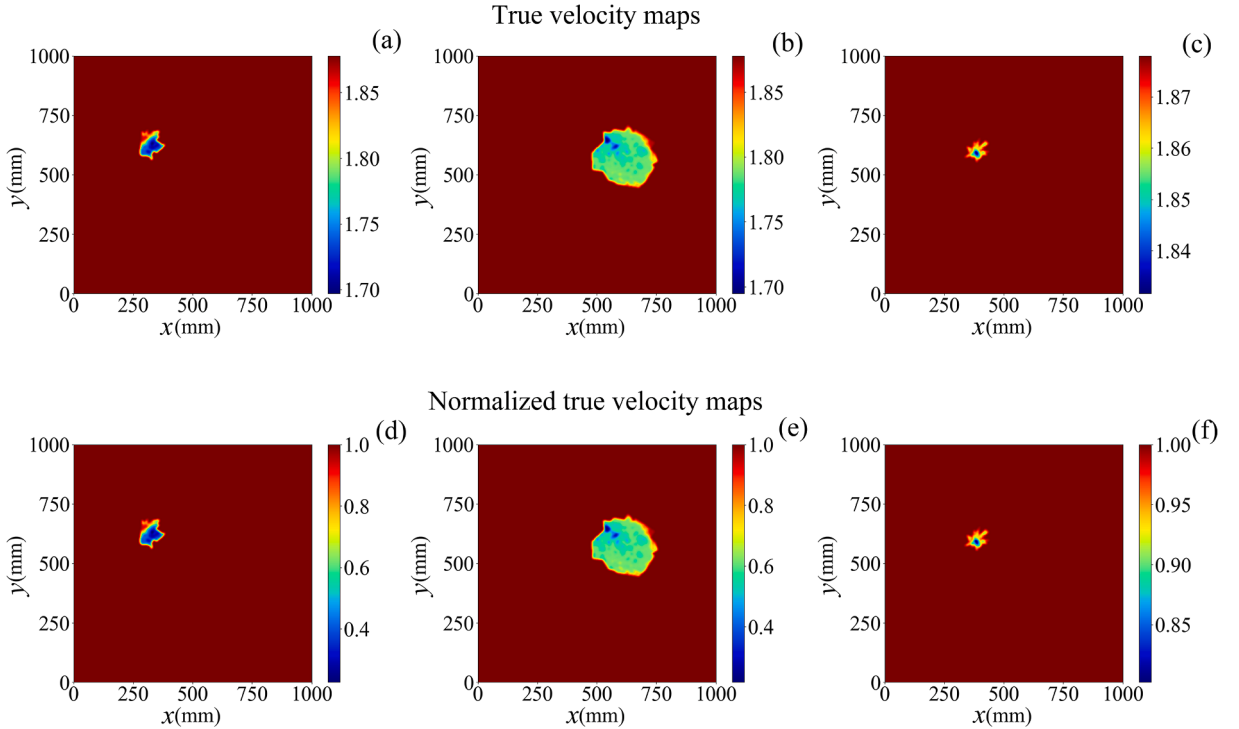


Fig. 4. (a), (b) and (c) the typical true velocity maps of aluminum plate, (d), (e) and (f) the normalized results of (a), (b) and (c). The corosions with different depth, shape and size are generated at random position on aluminum plate.

3.3. Numerical results

According to the principle of 1D-CNN mentioned in section II, the number of alternative convolutional and pooling layers is adjustable which will affect the imaging performance. Besides, the number and size of the convolution kernel, the size of max-pooling filter and the number of FC layer nodes are also of critical importance. Therefore, several network models with different hyper-parameters are trained, validated, and tested for optimal imaging models.

Except the hyper-parameters related to the network structure, some other hyper-parameters about training mechanism are shown in Table 2. In the training process, the batch size is set as 32 to ensure the training speed and prevent computer memory from overflowing. The total epoch and early stopping epoch are respectively specified as 1500 and 150, which means the stop condition of network training is that the total epoch is reached, or the validation loss does not decrease during 150 epochs. The model with the minimum validation loss rather than the model of the last training epoch is saved as the optimal model for corrosion imaging. In order to improve the generalization ability of the model, all the samples are shuffled before training. Furthermore, the training and validation set are also shuffled at the end of each epoch, and then the training and validation set are re-divided according to the allocation proportion rule mentioned.

3.4. CNN training and validation results of single corrosion damage

The feasibility of this imaging method is verified on the dataset containing single corrosion damage. Different numbers of alternative convolutional and pooling layers are adopted and some other hyper-parameter settings are listed in Table 3. Due to the large size of the one-dimensional input vectors, convolution kernel and pooling filter size should be large in the first alternating convolutional and pooling layer, so as to expand the receptive field to capture more information and to ensure the training speed simultaneously. As the numeric order of layer increases, the size of convolution kernel and pooling filter reduces and the number of convolution kernels increases for more detailed information. In order to accelerate training, a relatively small number of FC layer nodes is first attempted, which is specified as 64.

Fig. 5(a) and (b) show the training and validation loss of CNN with different numbers of alternating convolutional and pooling

Table 2
Summary of hyper-parameters about training mechanism.

	Total epoch	Early stopping epoch	Batch size
number	1500	150	32

Table 3

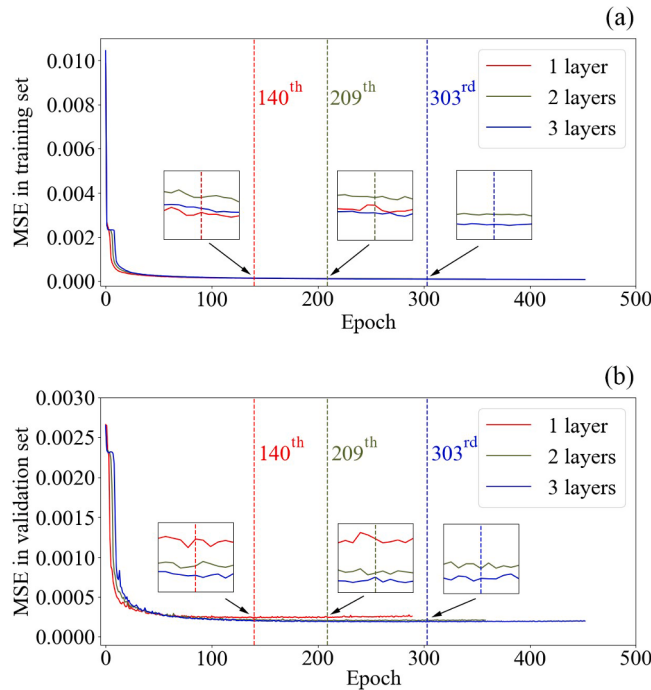
Summary of hyper-parameters when CNN models with different layers.

		Model 1 (1 layer)	Model 2 (2 layers)	Model 3 (3 layers)
C_1	Number	16	16	16
	Size	21	21	21
P_1	Size	5	5	5
			64	64
C_2	Number		15	15
	Size		4	4
P_2	Size			256
				9
P_3	Size			3
FC	Number of layers	1		
	Number of nodes	64		

'C' represents the convolutional layer.

'P' represents the pooling layer.

'FC' represents the fully connected layer.

**Fig. 5.** (a) The training, (b) validation loss of CNN with different number of alternating convolutional and pooling layers. The optimal models are respectively saved at the 140th, 209th and 303rd epochs.

layers. For each structure, the optimal models are respectively saved at the 140th, 209th and 303rd epochs. *MSEs* of the three models in training and validation tend to converge, declining rapidly at the beginning of training and slowly decreasing in the middle and late stages. Compared with network validation, the *MSE* convergence process in training is obviously more stable and smoother. With regard to convergence rate, model 1 converges faster than model 2 and model 3 at the beginning. However, due to the small number of layers, the *MSE* of model 1 no longer declines in the earlier epoch, resulting in large training and validation loss, which are 1.324×10^{-4} and 2.356×10^{-4} , respectively. The *MSEs* of model 2 and model 3 decline slowly and steadily, and the *MSE* of model 3 is the lowest both in training and validation, as demonstrated from the partially enlarged details. The training *MSEs* of model 2 and model 3 are respectively 1.246×10^{-4} , 9.410×10^{-5} , and the validation *MSEs* are respectively 2.015×10^{-4} and 1.876×10^{-4} . Considering the minimum training and validation *MSEs*, model 3 is optimal in the comparison of network layers.

A sample is randomly selected from the validation set, and the imaging results of the three models are shown in Fig. 6, in which the first and the second colorbar respectively represent the velocity and thickness of each point. The first and second columns are respectively the true maps and the imaging results, while the third column is the maximum *MSE* velocity profile fitting results along the x-axis. The dashed curve in the velocity profile represents the true velocity curves and the red curves are the fitting results. As shown in

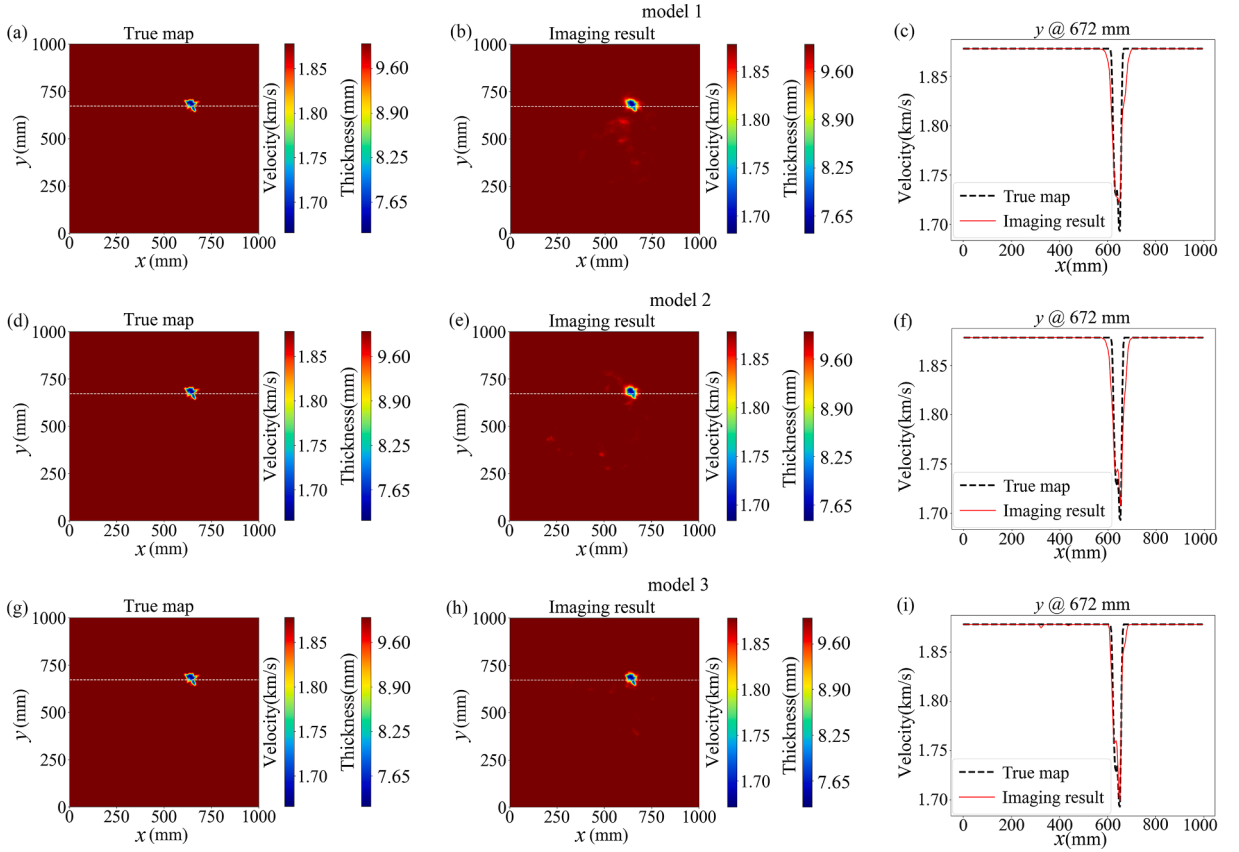


Fig. 6. A random sample in validation set (a) true map, (b) imaging result, (c) velocity profile fitting result of model 1, (d) true map, (e) imaging result, (f) velocity profile fitting result of model 2, (g) true map, (h) imaging result, (i) velocity profile fitting result of model 3, when CNN with different number of alternating convolutional and pooling layers.

Fig. 6, the shape, size, and position of corrosion damage in the validation sample can be predicted approximately. However, compared with model 3, more artifacts occur in the imaging results predicted by model 1 and model 2. In order to evaluate the velocity fitting results of each point, the maximum *MSE* velocity profile is checked. The fitting results of all three models are acceptable, but the maximum *MSE* velocity profile fits better with the increase of the number of layers. **Table 4** displays the quantitative imaging results of the random sample in the validation set and model 3 has lower *MSE* and velocity profile *MSE*.

In order to evaluate the similarity between the imaging results and the true velocity maps, the 2D correlation coefficient *r* is defined by extending the Pearson correlation coefficient:

$$r(v, s) = \frac{\text{Cov}(v, s)}{\sqrt{\text{Var}[v]\text{Var}[s]}} \quad (16)$$

where *v* represents the true velocity map matrix, *s* represents the predict velocity map matrix, *Cov* and *Var* are short for covariance and variance, respectively.

The correlation coefficient of the above random sample and the average correlation coefficient of the validation set are figured out to evaluate the overall imaging performance, as listed in the last two columns of **Table 4**. Besides, the average correlation coefficients of models 1, 2, and 3 in the training set are also calculated, which are respectively 0.8975, 0.9120 and 0.9304. Compared with model 1 and 2, the average correlation coefficient of model 3 is higher both in training and validation, which indicates that the models with

Table 4

The quantitative validation imaging results when CNN with different number of alternating convolutional and pooling layers.

	<i>MSE</i>	Velocity profile <i>MSE</i>	<i>r</i>	Average correlation coefficient
Model 1	4.39×10^{-6}	9.06×10^{-5}	0.9572	0.8843
Model 2	4.07×10^{-6}	1.20×10^{-4}	0.9603	0.8995
Model 3	1.41×10^{-6}	3.28×10^{-5}	0.9864	0.9154

more layers provide better corrosion damage reconstruction. When the number of alternating convolutional and pooling layers of CNN is fixed to 3, the number of nodes in the FC layer increases so as to determine the optimal network structure, and the specific setting is shown in **Table 5**. *MSEs* in training and validation are shown in **Fig. 7**, *MSE* converges smoothly in training, but fluctuates in validation. The optimal models of network with 64, 128 and 256 nodes in FC layer are saved at the 303rd, 375th and 287th epochs, respectively. With the number of nodes increasing, *MSE* is distinctly lower and is well illustrated by **Fig. 7**. The training *MSEs* of model 3, model 4 and model 5 are 9.410×10^{-5} , 5.58×10^{-5} and 4.91×10^{-5} , respectively, and the validation *MSEs* are 1.876×10^{-4} , 1.74×10^{-4} and 1.72×10^{-4} , respectively.

A sample is randomly selected from the validation set and its imaging results of three models with different number of nodes in FC layer is shown in **Fig. 8**. All the three models can accurately predict the size and position of corrosion damage and have almost no artifacts. However, the edge of corrosion damages is no longer clear and this phenomenon becomes more severe as the number of nodes in the FC layer decreases. The imaging performance of model 4 and model 5 are better according to internal velocity details of corrosion damage in **Figs. 8f** and **i**.

Table 6 displays the quantitative *MSE*, velocity profile *MSE* and correlation coefficient of the random sample when the number of layers is set as 3. The average correlation coefficient of the validation set is shown in the last column of **Table 6**. No matter for a single random sample in validation set or the total validation set, the imaging performance of model 5 is the best. Therefore, CNN with 3 layers and 256 nodes is determined as the optimal model.

3.5. CNN testing results of single corrosion damage

4000 extra samples which were not used in the training and validation are fed into model 5 for network testing. The Cumulative Distribution Function (CDF) of the correlation coefficient is shown in **Fig. 9**, in which CDF increases very slowly in the early stage and rapidly rises when the correlation coefficient is greater than or equal to 0.9, accounting for 82.73% of the testing set. This indicates that the number of samples with a high correlation coefficient is very large. The total *MSE* of the testing set and average correlation coefficient are 1.69×10^{-4} and 0.9262, respectively. This imaging method not only has excellent imaging performance, but the other advantage is that the imaging speed is extremely fast. The reconstruction time of 4000 samples is about 3 s on a single GPU computer (NVIDIA GeForce RTX 2080 Ti).

Fig. 10 is the visual imaging results, for which the first sample is the one with the smallest reconstruction error and the second sample is randomly selected from the testing set. Whatever the shape, size, position, and velocity of the corrosion damage, CNN can accurately predict which is proven from *MSE* and correlation coefficient. The *MSEs* of the two samples are 9.10×10^{-7} and 5.36×10^{-6} , and correlation coefficients are 0.9992 and 0.9887, respectively.

3.6. The influence of corrosion size on imaging performance

As the size of corrosion damage varies greatly, we present the investigation of the influence of corrosion size on imaging performance in this section. Statistical results are shown in **Fig. 11**, in which the x-axis represents the corrosion size and the y-axis represents the correlation coefficient of the imaging results. In order to simplify the definition of corrosion damage size, the corrosion damages are circles and the corrosion size is the ratio of the diameter to the wavelength. The minimum and the maximum corrosion size are one seventh wavelength and eleven wavelengths. As shown in the figure, when the corrosion size is small, the correlation coefficient of some samples is very low and the probability of low correlation coefficient is greater than that of large corrosion. Some corrosion damage samples with smaller sizes are tested. The quantitative results indicate that the accuracy of position detection is respectively 84%, 22%, and 2% when the corrosion damage size is close to $\lambda/2$, $2\lambda/7$ and $\lambda/7$. Therefore, this imaging method provides a reference for small corrosion damage detection. However, exceeding small corrosion damage imaging is very difficult when the corrosion damage size is less than two seventh wavelength.

The first and the second columns in **Fig. 12** are the visualization results of small damages with an approximate size of one half wavelength and two seventh wavelength. The first and the second rows represent the true maps and imaging results. In order to make imaging results more visible, the color bar is adjusted and the adjusted results are shown in the third row. As the corrosion size decreases, the prediction of size and shape becomes less accurate while the prediction of damage location is accurate.

3.7. Testing results of Anti-Noise interference

The dataset used in the above models does not contain noise, whereas the acquired detection signals are easily polluted by noise in actual conditions. In order to simulate the real condition as closely as possible, Gaussian noise is added to the original signals. The network structure and parameters are adjusted, and the model is retrained based on the dataset with noise. **Fig. 13** shows the testing result of a sample with a relatively high correlation coefficient. The size and position of corrosion can be predicted accurately.

Table 5

Summary of hyper-parameters when CNN models with different nodes in the FC layer.

	Model 3	Model 4	Model 5
The number of nodes in the FC layer	64	128	256

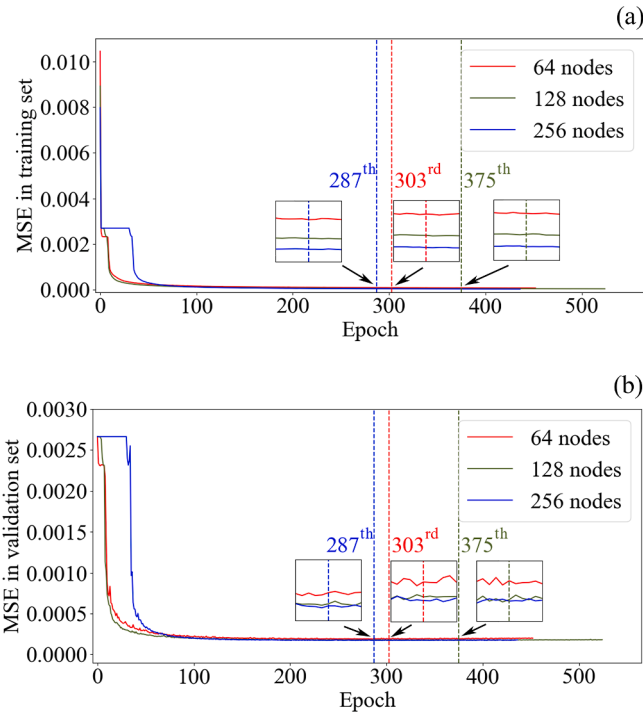


Fig. 7. (a) The training, (b) validation loss when the number of nodes in FC layer is different. The optimal models of three CNNs are saved at the 303rd, 375th and 287th epochs.

Although the prediction performance of the shape and internal velocity of corrosion is not perfect, it is acceptable. The *MSE*, correlation coefficient and velocity profile *MSE* of this sample are 1.97×10^{-5} , 0.9733 and 1.54×10^{-4} . The reason is that CNN also extracts the features of the noise, which is considered as useful information, resulting in slightly compromised imaging quality.

3.8. Experiment results

In order to verify the validity of this imaging method, an experiment was carried out and the experiment setup is approximately consistent with the simulation. 64 piezoelectric transducers (PZT-5H) were arranged into a uniform circular array with a diameter of 0.7 m and attached to a 6061-T6 aluminum plate with a size of 1000 mm × 1000 mm × 10 mm by methacrylate glue. The damages were manufactured on aluminum plate by CNC type planar milling machine, and the manufacturing accuracy was within 0.05 mm. A Coded Ultrasonic Imaging System (CUI-16 system) was used to generate and acquire data signals according to the transmitting-receiving criterion in the experiment. The imaging was conducted on a HP-Z8-G4 workstation with three NVIDIA RTX 2080Ti graphical processing unit (GPU) working parallelly.

Since the detection signals are in the time domain, it should be converted to the frequency domain and then the amplitude is extracted as the feature when frequencies are 35, 45, and 60 kHz. The dataset is enriched to enhance the robustness of the network, including experimental samples with different inversion frequencies, as well as simulation samples. The depth of corrosion damage is also deeper so that v_{min} is modified to 0. After the flattening and normalization and of the feature matrix, the preprocessed feature matrix is input into the network which is trained by the mixed simulation and experiment dataset for corrosion imaging.

Fig. 14a shows the simulated actual corrosion on an aluminum plate, its shape is irregular and the corrosion depth varies at different positions. According to the principle of velocity to thickness transformation, the true thickness map is transformed to velocity map, as shown in Fig. 14b. Fig. 14d is one of the most visible imaging results, in which the position is close to the actual position in true map. Since the lab experimental data is less than the numerical experimental data, CNN captures more features of the numerical experimental data. In addition, the features of numerical experimental data cannot be completely regarded as the features of lab experimental data due to the differences between numerical experimental data and lab experimental data. Moreover, the basic principle of this CNN model is to find a continuous mapping from observed data space to the phase velocity map of the aluminum plate. Because at the edges of the damages there are sharp variations in thickness, no functions with continuous derivatives can perfectly match thickness variations at these positions, which makes the imaging problem highly nonlinear and results in discrepancies between the reconstructed thickness map and true thickness map. This factor also indicates that the CNN model might have better performances in fitting corrosion damages with continuous thickness variations, where the robustness of this method is proved because in real environments damages with continuous thickness variation are more common. In terms of the cross-section velocity distributions, the maximum depth of corrosion is shallower than the actual depth, as shown in Fig. 14c. The *MSE*, correlation coefficient and velocity

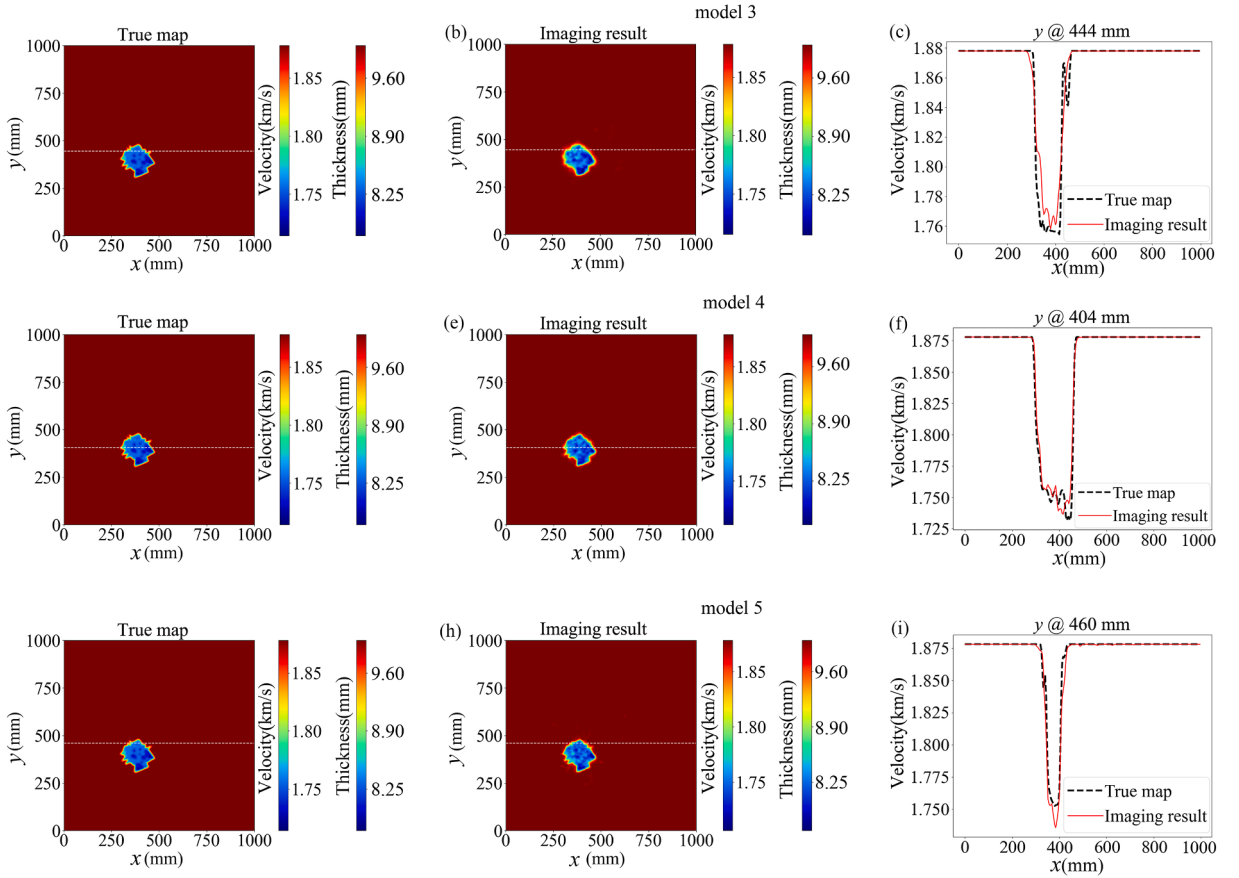


Fig. 8. The random sample in validation set (a) true map, (b) imaging result, (c) velocity profile fitting result of model 3, (d) true map, (e) imaging result, (f) velocity profile fitting result of model 4, (g) true map, (h) imaging result, (i) velocity profile fitting result of model 5, when the number of nodes in FC layer is different.

Table 6

The quantitative validation imaging results when the number of nodes in FC layer is different.

	MSE	Velocity profile MSE	r	Average correlation coefficient
Model 3	6.62×10^{-6}	7.21×10^{-5}	0.9875	0.9154
Model 4	2.60×10^{-6}	2.89×10^{-5}	0.9952	0.9251
Model 5	1.92×10^{-5}	2.59×10^{-5}	0.9965	0.9273

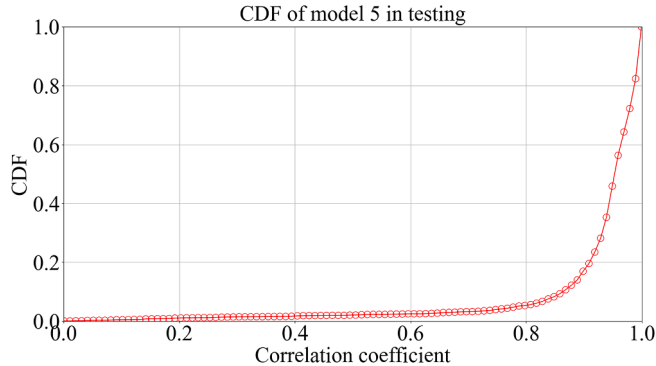


Fig. 9. The CDF of correlation coefficient in testing. The correlation coefficient greater than or equal to 0.9 accounts for 82.73% of the testing set.

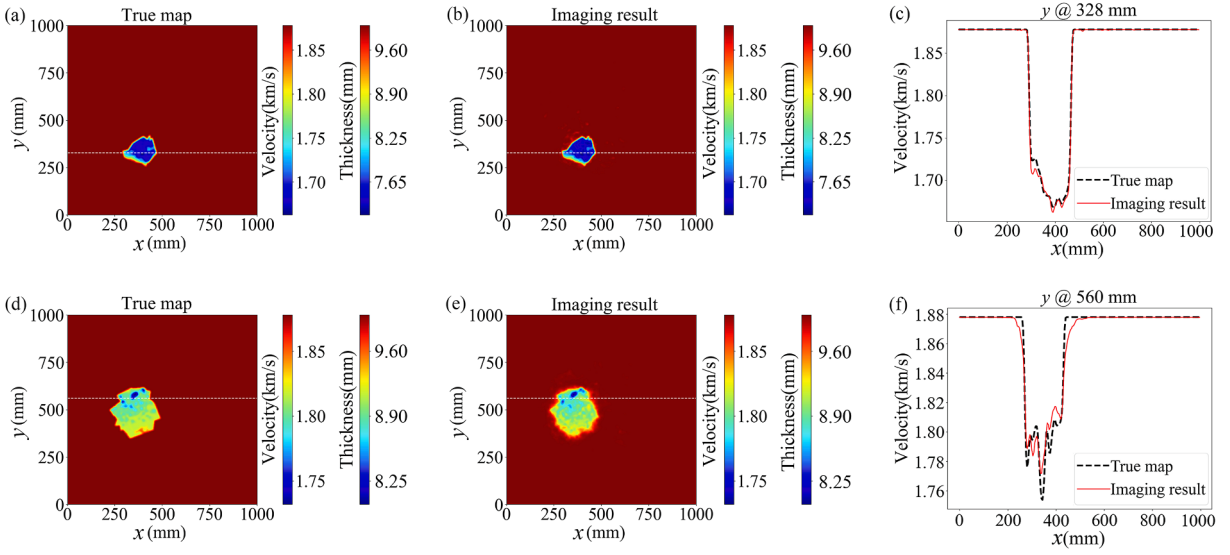


Fig. 10. The imaging results in testing set. (a) true map, (b) imaging result, (c) velocity profile fitting result of the one with the smallest reconstruction error, (d) true map, (e) imaging result, (f) velocity profile fitting result of the one randomly selected from the testing set.

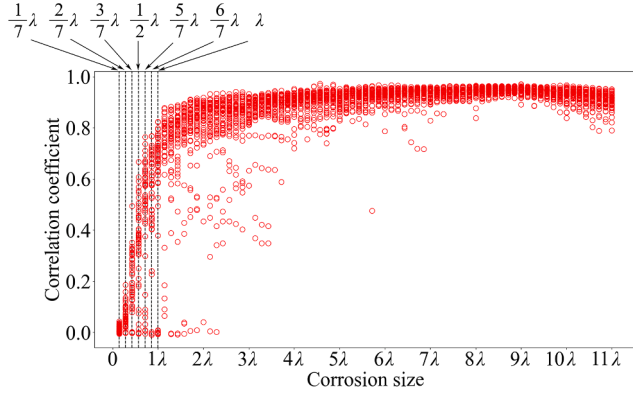


Fig. 11. Statistical results of the influence of corrosion size on image performance. The imaging quality of small corrosion is slightly worse, and the imaging quality of large corrosion is good.

profile MSE are respectively 7.37×10^{-5} , 0.9109 and 6.48×10^{-4} . The experimental results exhibit high resistance to noise, indicating that most of the detection signal features can be captured by CNN.

The database is changed again and the network is trained 20 times to prove that the success of the imaging method is not accidental. An experimental sample is fed into 20 trained models and the statistical results are shown in Fig. 15. The correlation coefficients are greater than 0.9, indicating that all of the models can successfully image the experimental sample, which demonstrates the great potentials for field applications. In addition, the program execution time and imaging accuracy of the CNN model proves that by combining with workstation having greater computation power and improvements in algorithms, the current model has the full potential to achieve real-time thickness mapping in the future.

4. Summary

A rapid guided wave imaging method based on CNN for quantitative corrosion evaluation is proposed in this paper. In the forward model, the true map of corrosion damage on the plate structure is known. According to the forward modeling of 2D wave equation, the detection signals can be calculated. Based on forward modeling data, the relationship between the detection signals and the velocity map is established by CNN training. Then, the trained model can be used for online corrosion imaging when the detection signals are inputted into the model. All the data should be normalized to eliminate the difference between amplitude before training. Adam algorithm is used to accelerate network training. Different numbers of alternating convolutional and pooling layers and FC layer nodes are adjusted for the optimal imaging model. Numerical experiment results demonstrate that CNN with 3 alternative convolutional and pooling layers and 256 nodes in the FC layer can imaging best. The average correlation coefficients are respectively 0.9493, 0.9273,

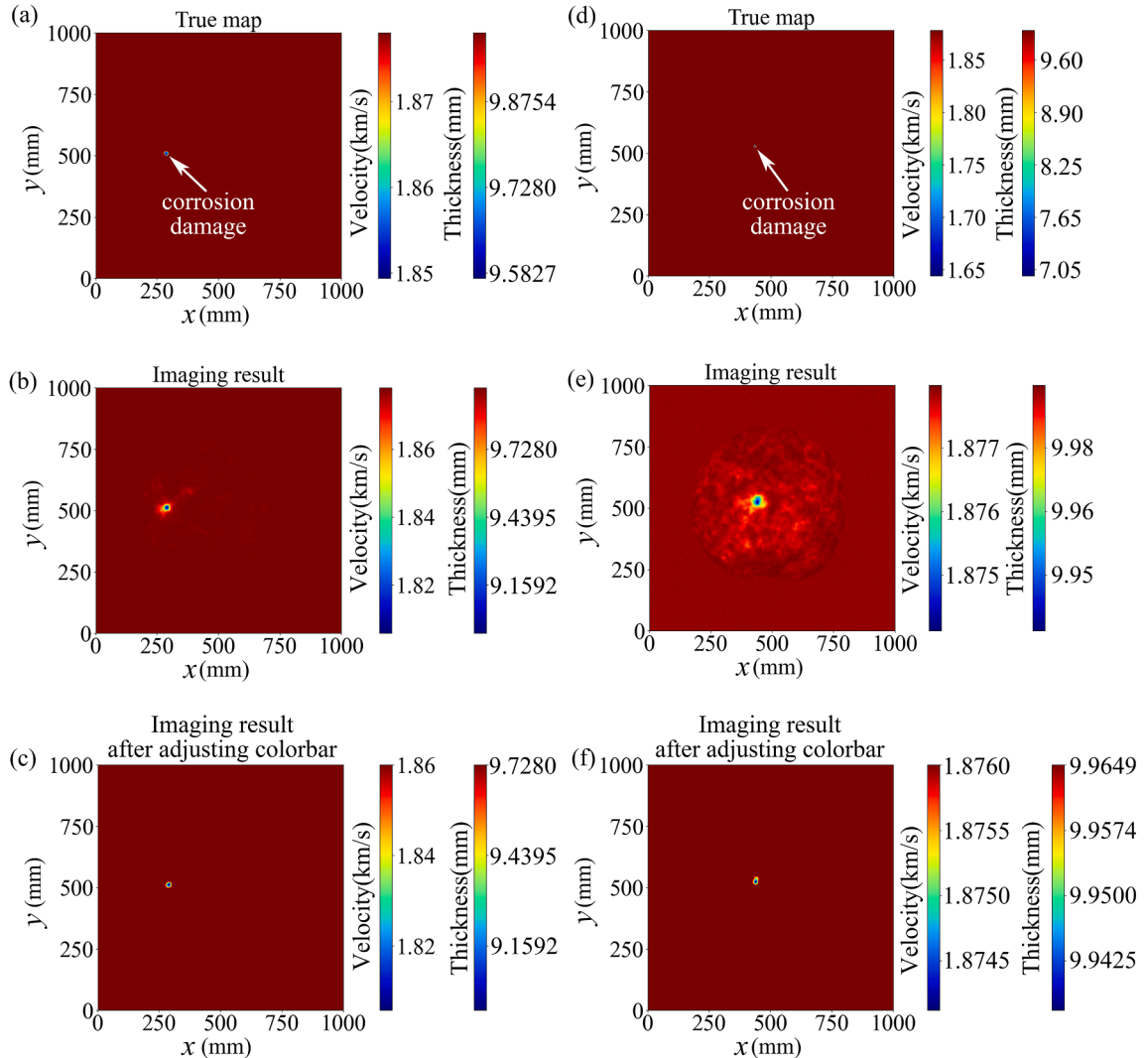


Fig. 12. (a) True map, (b) imaging result, (c) adjusted imaging result when corrosion size is close to one-half wavelength, (d) true map, (e) imaging result, (f) adjusted imaging result when corrosion size equals to two seventh wavelength.

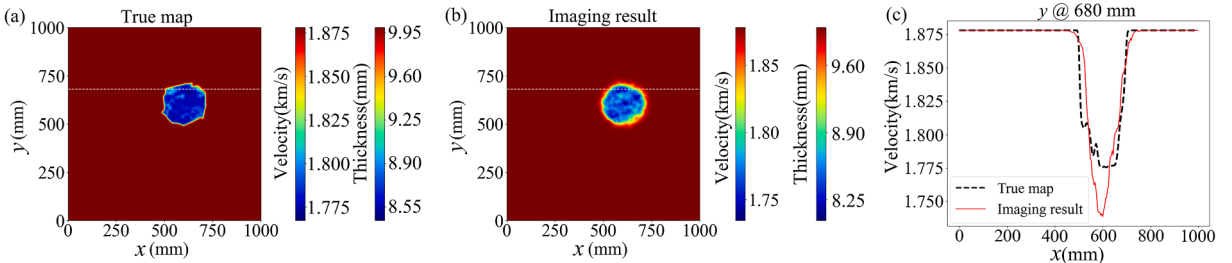


Fig. 13. (a) True map, (b) imaging result, (c) velocity profile fitting result of the testing sample with Gaussian noise. The size and position of corrosion can be predicted accurately, but the prediction performance of the shape and internal velocity of corrosion is not satisfactory.

and 0.9262 in training, validation, and testing. If the correlation coefficient greater than or equal to 0.9 is used as the criterion for the success of corrosion imaging, the success rate of applying the trained model to the testing set is 82.73%, showing excellent imaging performance. In terms of computational performance, imaging 4000 samples costs about 3 s on a single GPU computer, which is very efficient. Besides, the influence of corrosion size on imaging performance is studied, the image quality becomes better with the size

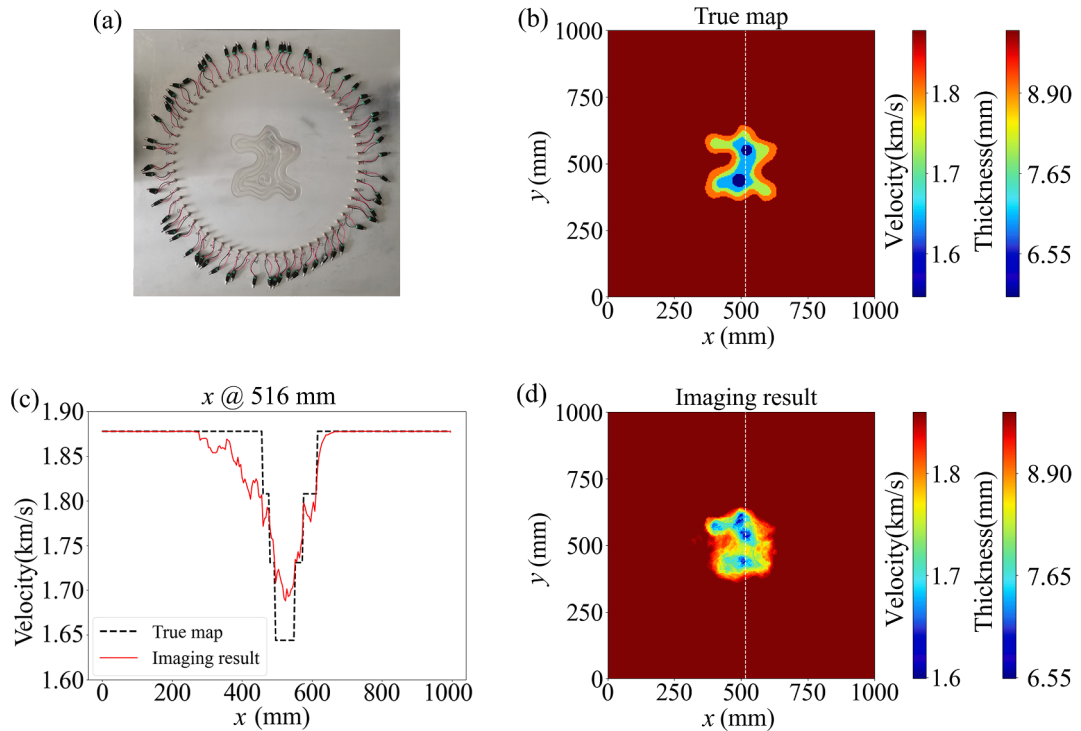


Fig. 14. (a) Aluminum plate and experiment configuration, (b) true map, (c) velocity profile fitting result and (d) the imaging result.

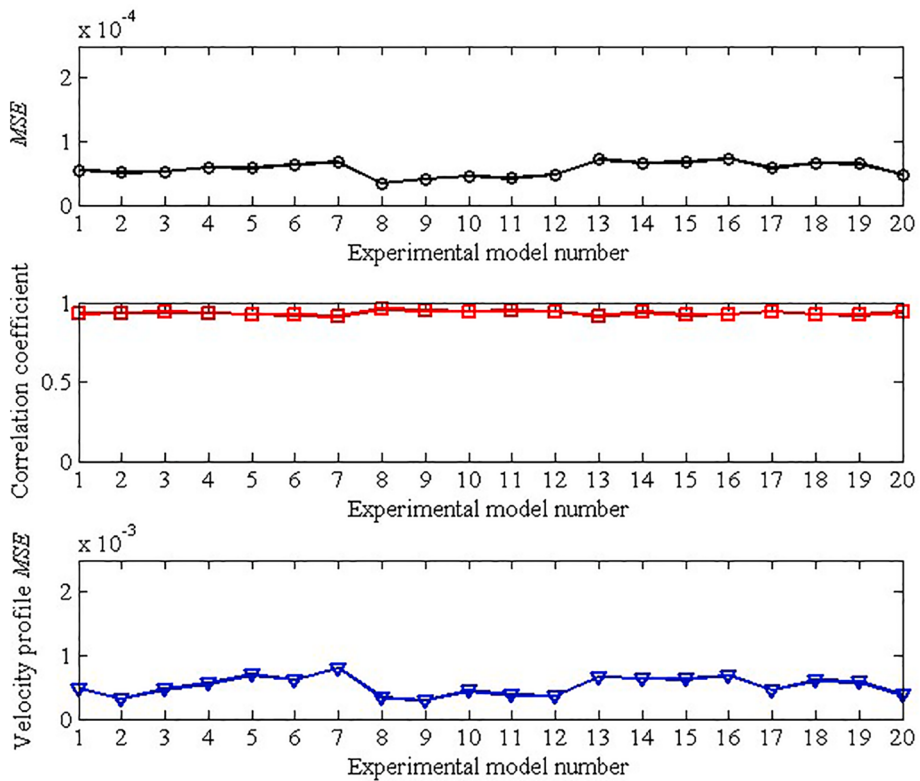


Fig. 15. Statistical results of experimental sample imaging.

increasing. The anti-noise ability of the model is tested and the results exhibit high resistance to noise. Although the prediction performance of the shape and internal velocity of corrosion is not perfect, the size and position of corrosion can be predicted accurately. Finally, lab experiments have been conducted and the imaging method was applied to the measured data. The result shows that the correlation coefficient between the true velocity map and the imaging result is 0.9109, which proves the imaging method is effective for practical applications.

Declaration of Competing Interest

The authors declare that they have no known competing financial interests or personal relationships that could have appeared to influence the work reported in this paper.

Acknowledgements

This work was supported in part by the National Science Foundation of China under contract number 61773283, in part by National Key R&D Program of China under contract number 2018YFC0808600.

References

- [1] S. Ragunath, C. Velmurugan, T. Kannan, Experimental investigation on corrosive behavior of boiler material using polarization technique, Procedia Mater. Sci. 5 (2014) 1274–1280, <https://doi.org/10.1016/j.mspro.2014.07.439>.
- [2] V.V. Zav'yaylov, Corrosion of oil-field pipelines, Prot. Met. 39 (3) (2003) 274–277, <https://doi.org/10.1023/A:1023975422504>.
- [3] R.A. Cole, Corrosion prevention in the aerospace industries, Anti-Corros. Methods Mater. 7 (10) (1960) 320–324, <https://doi.org/10.1108/eb019774>.
- [4] V Agarwala, P Reed, S Ahmad, "Corrosion Detection and Monitoring - A Review," Paper presented at the CORROSION 2000, Orlando, Florida, March 2000.
- [5] B Hou, "The Cost of Corrosion in China," npj Mater Degrad 1, 4 (2017). 10.1007/978-981-32-9354-0.
- [6] E.J. Richard, S A Vinod, "Fluorescence based chemical sensors for corrosion detection," In NACE - International Corrosion Conference Series (Vol. 1997-March). National Assoc. of Corrosion Engineers International.
- [7] A. Saini, H. Messenger, L. Kisley, Fluorophores "turned-on" by corrosion reactions can be detected at the single-molecule level, ACS Appl. Mater. Interfaces 13 (1) (2020), <https://doi.org/10.1021/acsami.0c18994>.
- [8] J. Lv, Q.X. Yue, R. Ding, et al., Intelligent anti-corrosion and corrosion detection coatings based on layered supramolecules intercalated by fluorescent off-on probes, J. Taiwan Inst. Chem. Eng. 118 (2021) 309–324, <https://doi.org/10.1016/j.jtice.2020.12.032>.
- [9] N. Vahdati, X. Wang, O. Shirayev, P. Rostron, F.F. Yap, External corrosion detection of oil pipelines using fiber optics, Sensors 20 (3) (2020) 684, <https://doi.org/10.3390/s20030684>.
- [10] J. Mao, J. Chen, C. Lei, et al., Monitoring the corrosion process of reinforced concrete using BOTDA and FBG sensors, Sensors (Basel, Switzerland) 15 (4) (2015), <https://doi.org/10.3390/s150408866>.
- [11] M.K. Elbataony, J. Mangual, P.H. Ziehl, et al., Early corrosion detection in prestressed concrete girders using acoustic emission, J. Mater. Civ. Eng. 26 (3) (2014) 504–511, [https://doi.org/10.1061/\(ASCE\)MT.1943-5533.0000845](https://doi.org/10.1061/(ASCE)MT.1943-5533.0000845).
- [12] G. Du, W. Wang, S. Song, et al., Detection of corrosion on 304 stainless steel by acoustic emission measurement, Anti-Corros. Methods Mater. 57 (3) (2010) 126–132, <https://doi.org/10.1108/00035591011040083>.
- [13] K. Wu, J.-Y. Kim, Acoustic emission monitoring during open-morphological pitting corrosion of 304 stainless steel passivated in dilute nitric acid, Corros. Sci. 180 (2021) 109224, <https://doi.org/10.1016/j.corsci.2020.109224>.
- [14] Y Ohara, H Endo, T Mihara, et al., "Ultrasonic Measurement of Closed Stress Corrosion Crack Depth Using Subharmonic Phased Array," Japanese Journal of Applied Physics, 48(7issue2): 07GD01-07GD01-6 (2009). 10.1143/JJAP.48.07GD01.
- [15] A. J. Hayman et al., "Quantitative corrosion evaluation in wells using a multi-function ultrasonic imager," 1995 IEEE Ultrasonics Symposium. Proceedings. An International Symposium, 1995, pp. 1115-1120 vol.2, 10.1109/ULTSYM.1995.495756.
- [16] C.D.S. Padilha, S. Thomasz, R.G.D.S. Araujo, *New Approach on Cement Evaluation for Oil and Gas Reservoirs Using Ultrasonic Images*, Rio de Janeiro, Brazil, August, 1997.
- [17] R Lasser, M Lasser, J Gurney, et al., "Large Area, Real Time Inspection Industrial Structures Using a Novel Handheld Ultrasound Camera// ASNT(American Society for Nondestructive Testing) Fall Conference & Quality Testing Show 2004: Paper Summaries. Imperium, Inc. 1738 Elton Road, #218 Silver Spring, MD 20903, 2004.
- [18] R.C. Sriramadasu, S. Banerjee, Y. Lu, Detection and assessment of pitting corrosion in rebars using scattering of ultrasonic guided waves, NDT & E Int. 101 (2018) 53–61, <https://doi.org/10.1016/j.ndteint.2018.10.005>.
- [19] A. Sharma, S. Sharma, S. Sharma, A. Mukherjee, Monitoring invisible corrosion in concrete using a combination of wave propagation techniques, Cem. Compos. 90 (2018) 89–99, <https://doi.org/10.1016/j.cemconcomp.2018.03.014>.
- [20] A. Farhidzadeh, S. Salamone, Reference-free corrosion damage diagnosis in steel strands using guided ultrasonic waves, Ultrasonics 57 (2015) 198–208, <https://doi.org/10.1016/j.ultras.2014.11.011>.
- [21] L. Mazeika, R. Kazys, R. Raisutis, et al., Ultrasonic guided wave tomography for the inspection of the fuel tanks floor, Int. J. Mater. Prod. Technol. 41 (1) (2011) 128–139, <https://doi.org/10.1504/IJMPT.2011.040291>.
- [22] J. Rao, M. Ratassepp, D. Lisevych, et al., On-line corrosion monitoring of plate structures based on guided wave tomography using piezoelectric sensors, Sensors 17 (12) (2017) 2882, <https://doi.org/10.3390/s17122882>.
- [23] J. Rao, M. Ratassepp, Z. Fan, Limited-view ultrasonic guided wave tomography using an adaptive regularization method, J. Appl. Phys. 120 (19) (2016) 113–127, <https://doi.org/10.1063/1.4967790>.
- [24] P. Huthwaite, F. Simonetti, High-resolution guided wave tomography, Wave Motion 50 (5) (2013) 979–993, <https://doi.org/10.1016/j.wavemoti.2013.04.004>.
- [25] C.L. Willey, F. Simonetti, P.B. Nagy, et al., Guided wave tomography of pipes with high-order helical modes, NDT & E Int. 65 (2014) 8–21, <https://doi.org/10.1016/j.ndteint.2014.03.010>.
- [26] J. Park, Y. Cho, A study on guided wave tomographic imaging for defects on a curved structure, J. Visualization 22 (6) (2019) 1081–1092, <https://doi.org/10.1007/s12650-019-00589-y>.
- [27] J. He, D.C. Rocha, P. Sava, Guided wave tomography based on least-squares reverse-time migration, Struct. Health Monitor. 19 (4) (2020) 1237–1249, <https://doi.org/10.1177/1475921719880296>.
- [28] L. Xu, S. Yuan, J. Chen, et al., Guided wave-convolutional neural network based fatigue crack diagnosis of aircraft structures, Sensors 19 (16) (2019) 3567, <https://doi.org/10.3390/s19163567>.
- [29] H. Liu, Y. Zhang, Deep learning based crack damage detection technique for thin plate structures using guided lamb wave signals, Smart Mater. Struct. 29 (1) (2020) 015032, <https://doi.org/10.1088/1361-665X/ab58d6>.
- [30] H Song, Y Yang, "Super-resolution visualization of subwavelength defects via deep learning-enhanced ultrasonic beamforming: A proof-of-principle study," NDT & E International, 116: 102344 (2020) 10.1016/j.ndteint.2020.102344.

- [31] H. Song, Y. Yang, Noncontact super-resolution guided wave array imaging of subwavelength defects using a multiscale deep learning approach, *Struct. Health Monitor.* 20 (4) (2021) 1904–1923, <https://doi.org/10.1177/1475921720942958>.
- [32] K.J. Marfurt, Accuracy of finite-difference and finite-element modeling of the scalar and elastic wave equations, *Geophysics* 49 (4) (1984) 533–549, <https://doi.org/10.1190/1.1441689>.
- [33] J. Virieux, “P-SV wave propagation in heterogeneous media: Velocity-stress finite-difference method,” *Geophysics*, 51: 1933–1942 (1986) 10.1190/1.1441605.
- [34] R. Grossier, J. Virieux, S. Operto, Parsimonious finite-volume frequency-domain method for 2-D P - SV -wave modelling, *Geophys. J. Int.* 175 (2) (2008) 541–559, <https://doi.org/10.1111/j.1365-246X.2008.03839.x>.
- [35] T. Ince, S. Kiranyaz, L. Eren, et al., Real-time motor fault detection by 1D convolutional neural networks, *IEEE Trans. Ind. Electron.* 63 (11) (2016) 7067–7075, <https://doi.org/10.1109/TIE.2016.2582729>.
- [36] S.H. Wang, K. Muhammad, J. Hong, et al., Alcoholism identification via convolutional neural network based on parametric ReLU, dropout, and batch normalization, *Neural Comput. Appl.* 32 (3) (2020) 665–680, <https://doi.org/10.1007/s00521-018-3924-0>.
- [37] N. Sainath T, B Kingsbury, G Saon, et al. “Deep Convolutional Neural Networks for Large-scale Speech Tasks,” *Neural Networks*, 64: 39-48 (2015). 10.1016/j.neunet.2014.08.005.
- [38] D Kingma and J Ba, “Adam: a method for stochastic optimization,” In: Proceedings of the 3rd international conference on learning representations, San Diego, CA, 7-9 May 2015.
- [39] J.L. Rose, *Ultrasonic Guided Waves in Solid Media*, Cambridge University Press, 2014.
- [40] M. Lin, Y. Liu, Guided wave tomography based on supervised descent method for quantitative corrosion imaging, *IEEE Trans. Ultrason. Ferroelectr. Freq. Control* 68 (12) (2021) 3624–3636, <https://doi.org/10.1109/TUFFC.2021.3097080>.